Unveiling the Synergistic Effect of Amorphous CoW-Phospho-Borides for Overall Alkaline Water Electrolysis

Aniruddha Bhide[a], Suraj Gupta[b], Rinkoo Bhabal[a], Kishan Mali[c], Brajesh Bhagat[c], Alpa Dashora[c], Maulik Patel[d], Rohan Fernandes[a], Nainesh Patel[a]*

[a]Department of Physics and Electronics, Christ University, Bengaluru, 560029, India

[b]Advanced Materials Department, Jožef Stefan Institute, Jamova 39, 1000 Ljubljana, Slovenia

[c]Department of Physics, Faculty of Science, The Maharaja Sayajirao University of Baroda, Vadodara 390002, India

[d]School of Engineering, University of Liverpool, Liverpool, L69 3GH (United Kingdom)

*Corresponding author:

Dr. Nainesh Patel,

E-mail: nainesh.patel@christuniversity.in

Phone: +91 9967619600

Abstract

Amorphous transition-metal-phospho-borides (TMPBs) are emerging as a new class of hybrid bifunctional catalysts for water-splitting. The present work reports the discovery of CoWPB as a new promising material that adds to the smaller family of TMPBs. The optimized compositions, namely Co4WPB5 and Co2WPB1 could achieve 10 mA/cm^2 at just 72 mV and 262 mV of overpotentials for hydrogen evolution reaction (HER) and oxygen evolution reaction (OER), respectively, in 1M KOH. Furthermore, the catalyst showed good performance in a 2-electrode assembly (1.59 V for 10 mA/cm^2) with considerable stability (70 h stability, 10000 operating cycles). Detailed morphological and electrochemical characterizations unveiled insights into the role of all elements in catalyst's improved performance. The presence of W was found to be crucial in improving the electronic conductivity and charge redistribution, making CoWPB suitable for both HER and OER. In computational simulation analysis, two configurations with different atomic environments, namely, $CoWPB_H$ and $CoWPB_O$ were found to have the lowest calculated overpotentials for HER and OER, respectively. It was found that the surface P-sites in $CoWPB_H$ were HER-active while the Co-sites in $CoWPB_O$ were OER-active sites. The study presents new knowledge about active sites in such multi-component catalysts that will foster more advancement in the area of water electrolysis.

Keywords

Hydrogen energy, Bifunctional electrocatalyst, Catalysis, Water splitting, Phospho-borides, Amorphous catalyst

1. Introduction

To fulfill the increasing energy demands caused by the meteoric rise in the global population, green energy sources such as hydrogen (H_2) must be included in the energy mix.[1] H_2 has been accepted as an ideal energy carrier owing to its high energy density and the possibility of being a zero-carbon entity.[2] H_2 is also a crucial feedstock for steel, chemical, cement and similar other industries, adding to its significance.[3–5] There are several methods to produce H_2 but the cleanest one with practically zero carbon emission, producing the so-called 'green H_2' is electrocatalytic water-splitting.[6] Electrolysis of water is over a 100-year-old industrial technique but the recent unprecedented demand of H_2 has created the need for improved methods. Amongst the current commercial technologies, anion exchange membrane water electrolyzers (AEMWEs) hold an edge over the incumbent alkaline and acidic water electrolyzers, owing to their compact design and non-reliance on platinum group metal (PGM) based electrodes.[7] Moreover, they offer the promise of scaling up to the Terawatt scale, needed to power large communities and industries. However, one of the key challenges with AEMWEs is the unavailability of electrode materials that simultaneously show good efficiency and long-term stability, suitable for implementation in commercial stacks.

As the alkaline conditions in an AEMWE allow the use of non-noble metals, electrocatalysts belonging to the transition metal categories are promising candidates for making electrodes. Transition-metal-based nitrides, chalcogenides, phosphides, and borides are amongst the commonly used alkaline-stable electrocatalysts for hydrogen evolution reaction (HER) and oxygen evolution reaction (OER),[8–10] with each of them offering certain pros and cons. For instance transition-metal based electrocatalysts such as $La_{0.6}Sr_{0.4}Co_{0.9}Fe_{0.1}O_{3-\delta}$ perovskite,[11] Fe-CoP cage,[12] and Co-MnO_2[13] showed better OER activity while Co-Mo-P@C,[14] NG@Co@Zn,[15] MoNiS@NiS/CC[16] displayed better HER

activity. In the past few years, transition-metal phospho-borides (TMPBs) have been developed as a hybrid catalyst that combines the properties of transition-metal borides and phosphides. For instance, amorphous cobalt phospho-boride (CoPB) has been reported for HER and OER in alkaline electrolytes by various groups.[8–10] CoPB shows unique electronic behavior due to the re-distribution of electron density between Co, P, and B, leading to a HER mechanism different from that observed in pure borides or phosphides. It has been demonstrated theorotically[17] as well as experimentally[18–21] that amorphous electrocatalysts exhibit superior electrochemical activity in comparison to their crystalline counterparts. The enhanced electrochemical activity of amorphous structures is attributed to the presence of a large number of highly active uncoordinated multicatalytic sites and unique electronic behavior inherent in the amorphous nature.[8,22,23] Owing to their improved catalytic rates, other configurations of phospho-borides, such as NiPB, FePB, etc.[10] have also been reported. In the past, our group reported a bi-metallic phospho-boride catalyst in the form of CoMoPB[23] that exhibited ultra-low OER overpotential, making it one of the most active non-noble OER catalysts. After the initial report on bi-metallic phospho-borides, subsequent studies have unveiled a handful of other electrocatalysts (W,P-FeB[24], Co-Fe-B-P[25], P-doped $Co_3O_{4-\delta}$[26], B-doped Ni_2P[27], Fe-Ni-P-B-O Nanocages[28], NiVFe-B-P LDHs@NF[29]) that have demonstrated noteworthy performance for either HER or OER. Notably, recent research has also highlighted similar bimetallic TMPBs which exhibit bifunctionality for overall water splitting (Co-Fe-B-P[30], Co-Mo-B-P/CF[31], Ni-2Fe-BP[32], Ni-Fe-PB[33], CoPB/rGO[10]). While these electrocatalysts have yielded promising outcomes, it is worth noting that the underlying factors contributing to their exceptional performance have rarely been explored in these reports. Hence, there is a pressing need to recognize the role of each element and catalytic sites within these multi-component compounds, allowing for further refinement to achieve activity levels comparable to those observed in PGMs. In the

present study, an attempt has been made to get a deeper understanding of bi-metallic phospho-borides by employing a combination of computational simulation studies, alongside the customary electrochemical and morphological characterizations to pinpoint the exact active sites.

With a goal to design new materials that can go beyond the current state-of-the-art in metal phospho-borides and gain a fundamental understanding of this new class of hybrid electrocatalysts, we report the results obtained for new amorphous CoWPB electrocatalysts. W was chosen as the second metal due to its ability to enhance the conductivity of the material[22,34] and it also acts as an atomic barrier that helps in avoiding the agglomeration of the catalyst to improve the BET surface area.[22,35,36] These bimetallic phospho-boride were optimized and evaluated as a bifunctional electrocatalyst for HER and OER, in alkaline electrolytes. Different compositions of CoWPB showed remarkable performance for HER and OER, suggesting separate active sites for each reaction. A better understanding of the active sites in the complex amorphous structure of CoWPB and the specific role of each element was obtained through computational investigations. The discovery of this new member catalyst in the phospho-boride family and the new insights gained in this work will add to the missing knowledge about these materials and serve as exemplary in the future. This work will also showcase that easy to synthesize bi-metallic phospho-borides have the potential to achieve new benchmarks in electrocatalytic water-splitting, making them suitable for incorporation and upscaling in AEMWEs.

2. Material and methods

2.1. Experimental Sections

2.1.1. Materials:

Cobalt chloride hexahydrate ($CoCl_2.6H_2O$, 99%, Researchlab), sodium tungstate ($Na_2WO_4.2H_2O$, 98%, Researchlab), sodium hypophosphite ($NaH_2PO_2.H_2O$, 99%, Researchlab), sodium borohydride ($NaBH_4$, 98%, Researchlab), potassium hydroxide pellets (KOH, 99%, Researchlab), sodium hydroxide pellets (NaOH, 99%, Researchlab), ethanol (C_2H_5OH, 99%, Researchlab), acetone (C_3H_6O, 99%, Researchlab), Hydrochloric actid (HCl, 98%, Researchlab). Deionized (DI) water was used as the general-purpose solvent. Nickel foam was acquired from Dtech solutions, India.

2.1.2. Synthesis of electrocatalyst:

CoWPB catalyst powders were synthesized using the well-established chemical reduction method. An aqueous mixture of cobalt chloride ($CoCl_2.6H_2O$), sodium tungstate ($Na_2WO_4.2H_2O$) and sodium hypophosphite ($NaH_2PO_2.H_2O$) was prepared in desired molar ratios. To this mixture, an appropriate amount of sodium borohydride ($NaBH_4$) was added at once, under vigorous stirring. With the addition of $NaBH_4$, the color of the mixture turned black and effervescence was seen, which is an indicator of the instantaneous reduction of metal salts. Here, $NaBH_4$ plays a dual role, as the main reducing agent and also source of the boron. Based on previous reports,[8,17] the molar ratio (B+P)/Co (ratio of moles of B and P to metal precursors) was kept constant at three to ensure the complete reduction of Co and W. After 30 min of stirring, the effervescence ceases and the black precipitate was separated by centrifugation, followed by washing with deionized water and ethanol. To optimize the catalyst composition, the molar percentage of W/(Co+W) and B/P ratio were varied, as listed in **Table S1**. The various catalyst compositions will be represented as Co*x*WPB*y*, where *x* denotes the W/(Co+W) molar percentage and *y* denotes the B/P molar ratio. For instance, the catalyst with W/(Co+W) percentage of 4 and B/P ratio of 5 will be denoted as Co4WPB5. As a reference, Co*x*WB and CoPB*y* samples were also prepared using the same method but without the addition of P and W in the mixture, respectively.

2.1.3. Structural and morphological characterizations:

XRD (Rigaku miniflex) equipped with a radiation source of Cu Kα with λ =1.5441 nm was used in the θ-2θ configuration to analyze the crystallinity of the materials. The surface morphology and size distribution of the catalyst powders were identified using scanning electron microscopy (SEM, 7001F, JEOL) and scanning transmission electron microscope (STEM, JEOL 2100+). Selective area electron diffraction (SAED) patterns were also obtained using the same equipment. Electron dispersive spectroscopy (EDS) and X-ray photoelectron spectroscopy (XPS, Versaprobe III, PHI) were used to investigate the bulk and surface elemental composition, respectively. Brunauer, Emmett and Teller (BET) adsorption-desorption curves were obtained (Micrometric 3-Flex 3500 Gas Sorption Analyzer) to determine the specific surface area of the catalyst powders.

2.1.4. Fabrication of working electrode:

For the preparation of the working electrode, 5 mg of catalyst powder was mixed with 1 ml of ethanol and sonicated for 10 min to form a homogenous catalyst ink. Separately, 20 µl of Nafion was added in 0.5 ml ethanol and sonicated for 1 min to prepare the binder solution. Finally, 10 µl of binder solution was deposited onto the glassy carbon (GC) electrode (3 mm diameter, CH instruments), followed by 20 µl of catalyst ink, resulting in a loading of ~1.4 mg/cm^2. A similar process was used to deposit the catalysts on nickel foam (NF) substrate (1 cm X 0.5 cm), achieving a similar catalyst loading. Prior to deposition, NF was cleaned by ultrasonication in 1M NaOH, followed by acetone (5 min) to remove the oil, grease and other impurities on the surface[37–39]. After cleaning, the NF surface was activated by ultrasonication in 10% HCl solution (5 min). Finally, the activated NF was rinsed with DI water and dried in the air.

2.1.5. Electrochemical characterizations:

A conventional 3-electrode system was used to perform all the electrochemical characterizations using an electrochemical workstation (CHI6011E). The setup consisted of catalyst coated GC as the working electrode, a platinum counter electrode (2mm dia.) and a saturated calomel electrode (SCE) as the reference. 1M KOH (pH 14) was used as an electrolyte for all the measurements. To eliminate the possibility of Pt contamination and ascertain the repeatability of the obtained results, the electrochemical tests were also performed using a graphite rod as a counter electrode. The measured potentials were converted with respect to the reversible hydrogen electrode (RHE) by adding a value of +1.067 V,[8] according to the Nernst equation $E_{(RHE)} = E_{(SCE)}^{0} + 0.059*pH$ where $E_{(SCE)}^{0} = 0.241$ and pH = 14.

The linear polarization measurements for HER and OER were performed at a scan rate of 2 mV/s to minimize the background currents. The electrolyte was continuously stirred to avoid the accumulation of bubbles over the GC electrode and also minimize the mass transfer limitations. Prior to HER measurements, a constant reducing potential was applied to the working electrode until the current was stabilized. Likewise, prior to OER, the catalyst surface was activated by applying anodic linear potential at a scan rate of 2 mV/s, which also yielded the pre-OER oxidation peaks. The HER and OER experiments were repeated multiple times to ascertain the obtained data. Electrochemical impedance spectroscopy (EIS) was performed upon the activated catalyst to determine the solution (R_u) and charge transfer (R_{ct}) resistance. The measured value of R_u was used for iR compensation and the calculated values were manually subtracted from the observed potentials. Tafel slopes were calculated by linear fitting the graph obtained by plotting the log of current density log (i) against the overpotential (η). To determine the double layer capacitance (C_{DL}), cyclic voltammetry (CV) scans were recorded at different scan rates (20, 40, 60, 80, 100, 120 mV/s) in the non-

Faradaic range within ± 100 mV across the open circuit potential (OCP). Based on this graph, the difference in cathodic and anodic current densities at OCP (ΔJ) were plotted against the corresponding scan rates to determine the value of C_{DL}. Electrochemical active surface area (ECSA) was then calculated using **equation S1**. Turnover frequency (TOF) values were estimated using the method reported in previous work.[40]. Faradaic efficiency was obtained using the procedure mentioned in the supporting information. The long-term stability of the catalysts was assessed by performing chronoamperometric tests at a constant potential for 70 h and the recyclability of the catalyst was tested by recording LSVs for 10000 cycles at a scan rate of 100 mV/s on GC electrode. 2-electrode measurements were performed by directly using the most active CoWPB compositions as cathode and anode catalysts.

2.2. Computational Studies

Density functional theory-based QUANTUM ESPRESSO code,[41] with Perdew-Burke-Ernzerhof (PBE) generalized gradient approximation (GGA) [42] as an exchange-correlation functional was used for ground state energy calculations. Ultrasoft pseudopotential was used along with a plane wave cut-off of 60 Ry and a charge density cut-off of 600 Ry. For structural relaxation and electronic properties, a gamma-centered *k*-mesh grid of 4×4×1 and 8×8×1, was utilized, respectively. Initially, an amorphous model of Co-B with 64 atoms was developed using molecular dynamics (MD) simulation with Car-Parrinello dynamics.[43] Detailed procedure and simulation parameters are provided in our previous work.[22] The constructed amorphous structures contain forces and stresses as they are equilibrated at 300 K. In order to minimize the energy of the system, volume and position optimization was carried out with a force threshold of 10^{-3} Ry/Å. To assess catalytic activity, a threefold CoB site (TF-2CoB), as discovered in our previous work[22] to be the most active site, was exposed

by adopting a slab configuration based on the prepared amorphous CoB. This configuration included a 15 Å vacuum layer to mimic the slab model, thus eliminating any possible vertical interactions arising from periodic images. The incorporation of W atoms at Co sites was done according to previously reported optimized sites[22] which also served as the starting point for constructing CoWPB structures. The two CoWB models that provided the best sites for HER and OER labeled as $CoWB_H$ (**Fig. S1a**) and $CoWB_O$ (**Fig. S1b**) were chosen for incorporation of P atoms at B sites to obtain the amorphous CoWPB models. The B atoms that surround the most active TF-2CoB site (marked with a red star in **Fig. S1**) are substituted by P atoms. Four such B-sites were identified for substitution, as marked with red circles in **Fig. S1** and the sites are labeled as: (1) P_Co1, (2) P_Co2, (3) P_2Co, and (4) P_direct. Two different CoWB and four different possible sites for P incorporation led to the generation of 8 different structures of CoWPB. HER and OER were simulated over these 8 models, by considering Co or P as the active sites. Details regarding the calculation of Gibbs free energy and overpotential are provided in the Supporting Information.

3. Results and discussion

Owing to the presence of multiple elements in CoWPB, it becomes customary to identify the optimum concentration of metals (Co, W) and metalloid/non-metal (B, P) in CoWPB. To achieve this optimization, the ratio of elements in CoWPB was varied and the most optimum configuration was screened based on the overpotential values at 10 mA/cm^2 of current density for HER and OER (**Fig. S2, Table S1**). The sample with a W/(Co+W) molar concentration of 4% and B/P ratio of 5 (termed as Co4WPB5) showed the lowest HER overpotential while the one with W/(Co+W) molar concentration of 2% and B/P ratio of 1, termed as Co2WPB1, showed the lowest OER overpotential (**Table S1, Fig. S3**). Thus,

Co4WPB5 and Co2WPB1 were primarily used for all further characterization and analysis. The SEM images show that Co4WPB5 has agglomerated nanoparticle-like morphology

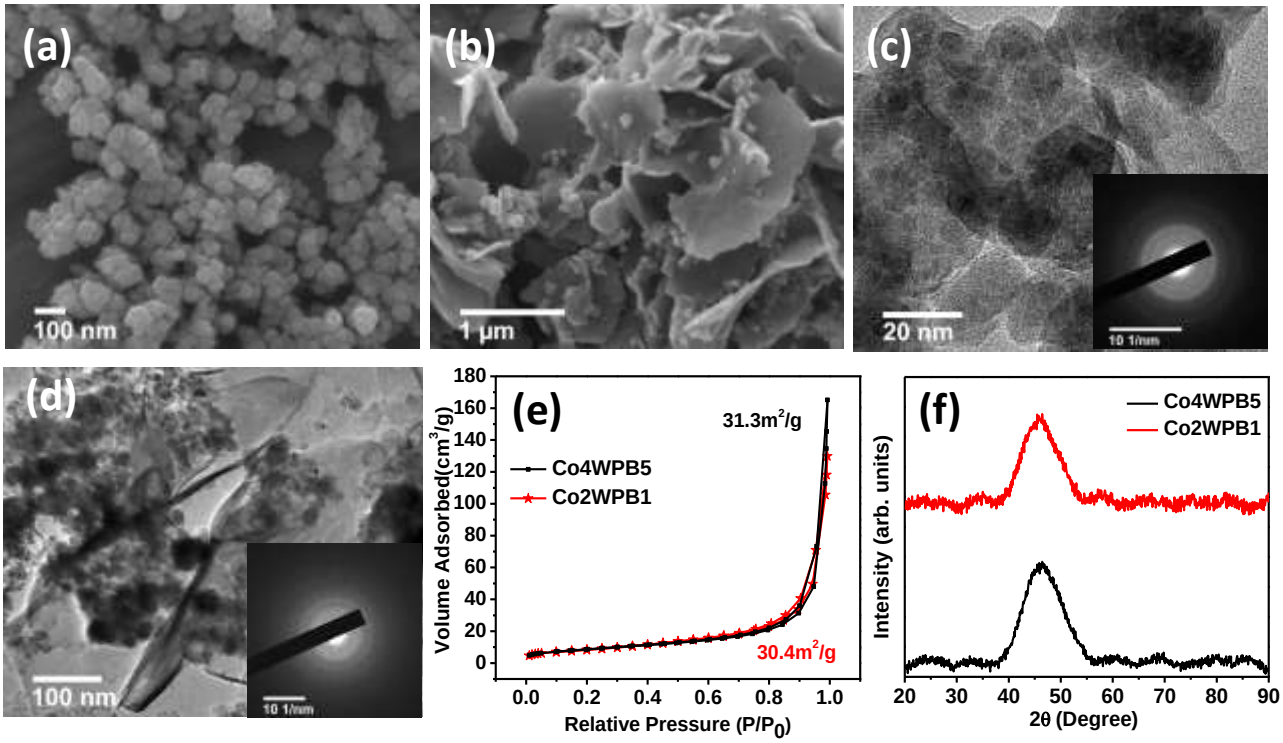

Figure 1: SEM images of **(a)** Co4WPB5 and **(b)** Co2WPB1 samples, TEM micrographs for **(c)** Co4WPB5 and **(d)** Co2WPB1 along with the corresponding diffraction patterns (inset), **(e)** N_2 adsorption-desorption isotherms and **(f)** XRD patterns for Co4WPB5 and Co2WPB1 electrocatalysts.

(**Fig. 1a**), while Co2WPB1 has nanoflake-like morphology along with small number of nanoparticles (**Fig. 1b**). The calculated size distribution (**Fig. S4**) shows an average particle size of 52.3 ± 5.4 nm for Co4WPB5 and average planar width of 43.4 ± 4.3 nm for Co2WPB1. The nanoparticulate and flake-like morphologies of Co4WPB5 and Co2WPB1, respectively, were also supported by their TEM micrographs (**Fig. 1c,d**). HRTEM images of Co4WPB5 and Co2WPB1 (**Fig. S6a, b**) show absence of any lattice fringes. It is noteworthy that the sources of B and P, i.e. $NaBH_4$ and NaH_2PO_2 are both reducing agents

but $NaBH_4$ is far stronger than NaH_2PO_2.[8] When $NaBH_4$ is used for such types of aqueous reduction reactions, it is generally observed that the reaction is exothermic and highly spontaneous, which leads to the formation of amorphous nanoparticles, as observed in several reports.[17,40] Here, a similar phenomenon was manifested in all the samples where only $NaBH_4$ was used, for instance in Co4WB and Co2WB (**Fig. S5a,b and S6c,d**). In the case of Co4WPB5, the molar ratio of $NaBH_4$ is 5 times higher than that of NaH_2PO_2 and hence the overall reaction rate is dictated by $NaBH_4$, leading to the formation of nanoparticles. A similar observation was made for the CoPB5 sample (**Fig. S5d and S6e**). Being a mild reducing agent, the reaction precedes slowly in presence of NaH_2PO_2 leading to the formation of flake-like morphology,[8] as also observed from the SEM image of CoP (**Fig. S5c**). Moreover, the flake-like morphology was persistently observed where an equal molar ratio of $NaBH_4$ and NaH_2PO_2 was used, such as in CoPB1 (**Fig. S5e and S6f**), and that explains the formation of flake-like morphology in Co2WPB1 (**Fig. 1b,d**). Though the nanoflake morphology is the dominant one, a small number of nanoparticles can also be seen that could be an effect of the competing reduction reaction with $NaBH_4$. Irrespective of their different morphologies, the specific surface area obtained from N_2 adsorption-desorption isotherms (**Fig. 1e**) showed similar values for both Co4WPB5 (31.3 m^2/g) and Co2WPB1 (30.4 m^2/g). Furthermore, when comparing the CoWPB catalysts with their counterparts (**Fig. S7**), it becomes evident that both CoWPB and CoWB exhibit significantly higher BET surface areas in comparison to CoPB, as well as the previously reported CoB catalyst (28.9 m^2/g).[17] This suggests that the introduction of W into CoPB and CoB has led to an increase in specific surface area, which can likely be attributed to a reduction in particle agglomeration, as W functions as an atomic barrier between the CoPB particles, similar to previously reported for CoWB.[22] SAED pattern obtained from TEM reveals diffused rings surrounding the central maxima in all the samples (inset in **Fig. 1c,d and S6c-f**). This

characteristic pattern indicates that the catalysts possess an amorphous nature. Such disordered structure was further supported by XRD pattern (**Fig. 1f and S8**) that clearly shows a single broad hump centered at 2θ = 45°, typical of amorphous metal borides.[8,22,40]

In such amorphous systems, identification of the elemental chemical states becomes even more important to predict the chemical properties of the catalyst. TEM-EDS maps for Co4WPB5 (**Fig. S9a)** and Co2WPB1 (**Fig. S9b)** show the uniform distribution of Co, W and P across the sample.

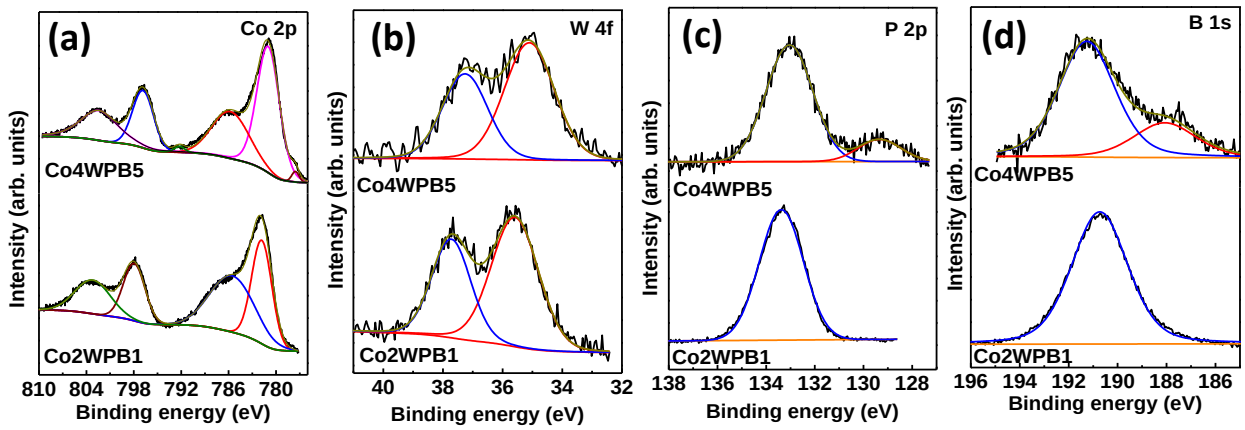

Figure 2: High-resolution XPS spectra for (a) Co 2p, (b) W 4f, (c) P 2p, and (d) B 1s levels in Co4WPB5 (upper panels) and Co2WPB1 (lower panels).

Owing to the detection limit of the EDS detector, the distribution of B could not be confirmed accurately as its atomic number is low and its signal overlaps predominantly with carbon.[44] For more precise identification of the surface chemical states, XPS was used and the atomic percentages of all elements present on the surface of Co4WPB5 and Co2WPB1 obtained from XPS are summarized in **Table S2.** In Co4WPB5, XPS spectra for $Co2p_{3/2}$ (**Fig. 2a, upper panel**) display two peaks at binding energy (BE) of 777.8 eV and 781.0 eV, representing the metallic Co^0 as well as oxidized Co^{3+} state, respectively.[45] A higher energy satellite peak was observed at 785.7 eV. The similar set of peaks corresponding to metallic and oxidized Co in the Co $2p_{1/2}$ level were also observed.[45] Deconvolution of W 4f level (**Fig. 2b, upper panel**) results in two peaks with BEs of 35.1 eV and 37.2 eV, both of which

correspond to the oxidized W^{6+} state.[22] For the P 2p level (**Fig. 2c, upper panel**) the spectra depict an elemental P^0 peak (129.3 eV) and an oxidized peak (133.0 eV) belonging to orthophosphate functional group.[8,46] Likewise, the deconvoluted B1s levels (**Fig. 2d, upper panel**) display peaks at 188.0 eV corresponding to elemental B (B^0) while the peak at 191.2 eV corresponds to oxidized B_2O_3.[8] Moreover, the Co^0 and P^0 peaks were negatively shifted by 0.3 eV and 0.6 eV, respectively, compared to their pure elemental states (778.1 and 129.9 eV respectively).[8] On the other hand, B^0 peak was positively shifted by 0.9 eV from that of pure B (187.1 eV),[17] confirming the interplay of electronic charges between Co, P, and B that eventually might modulate the H-adsorption energies at the active sites. This characteristic charge transfer can also be observed in CoPB and CoWB electrocatalysts (**Fig. S10**). The CoPB displays a negative shift of 0.6 eV in P^0 peak (129.6 eV) of P 2p state and a positive shift of 0.9 eV in B^0 peak (188.0 eV) of the B 1s state. Similarly, the B 1s state of CoWB shows a positive shift of 0.8 eV in B^0 peak (187.8 eV). The negative shift in BE of Co and P (positive shift in BE of B) represents a gain of electrons (loss of electrons), a characteristic phenomenon observed in transition metal borides and phosphides.[8,17,22] Such modulation of electronic charge may create optimal active sites for HER reaction. The XPS spectra of Co2WPB1 show similar features as Co4WPB5 but with a few key exceptions. For instance, Co $2P_{3/2}$ spectra of Co2WPB1 (**Fig. 2a, lower panel**) show no evidence of metallic Co^0 and Co exists only in the oxidized Co^{3+} state (781.8 eV). In comparison to Co4WPB5, the peak attributed to Co^{3+} state is positively shifted for Co2WPB1 thus suggesting a higher degree of oxidation. W 4f spectra (**Fig. 2b, lower panel**) show BE peaks at 35.5 eV and 37.7 eV suggesting the existence of W in the oxidized form. For P 2p (**Fig. 2c, lower panel**) and B 1s (**Fig. 2d, lower panel**) states, again no elemental peaks were present and only those corresponding to oxidized states were noticed. The presence of all the elements in their oxidized states could potentially be advantageous for the OER, as it involves the

transformation of catalyst surfaces into higher oxidation state species. The absence of electronic charge modulation in Co2WPB1, in contrast to Co4WPB5, suggests that the existence of complementary active sites on the surface of CoWPB are controlled by the B/P ratio as well as W/(W+Co) ratio.

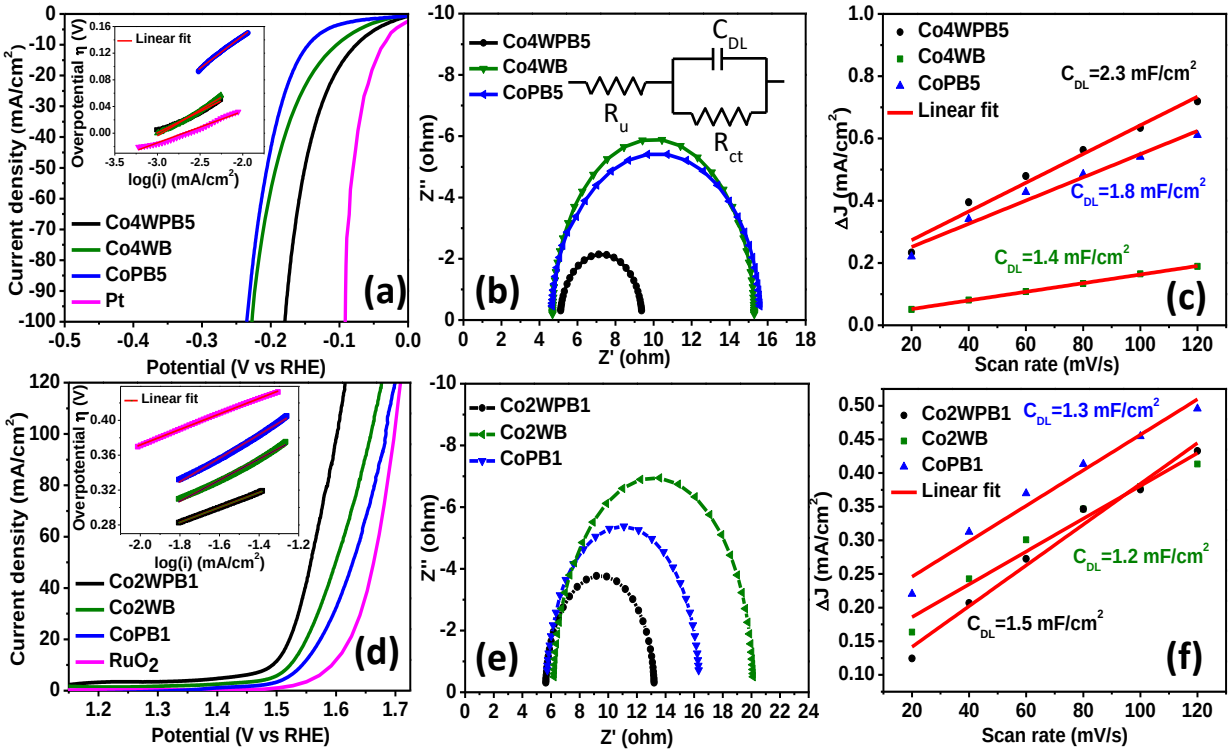

Figure 3: (a) Cathodic polarization curves (inset shows the corresponding Tafel plots), **(b)** Nyquist plots (with the equivalent fitting circuit as an inset) at - 0.15 V vs RHE, and **(c)** Plot of ΔJ (at OCP) vs scan rate for Co4WPB5 along with the reference catalysts (Co4WB, and CoPB5) in 1 M KOH. **(d)** Anodic polarization curves (inset shows the corresponding Tafel plots), **(e)** Nyquist plots at 1.66 V vs RHE, and **(f)** Plot of ΔJ (at OCP) vs scan rate for Co2WPB1 along with the reference catalysts (Co2WB, and CoPB1) in 1 M KOH.

The electrochemical screening of the different catalyst compositions (**Fig. S2a, S3a,** and **Table S1**) for HER was performed by subjecting them to cathodic polarization, and the overpotential required to achieve 10 mA/cm^2 (η_{10}) was used as the key metric for

comparison. **Fig. 3a** shows the LSV scan for the best HER composition (Co4WPB5) along with that for the reference electrocatalysts (Co4WB, CoPB5 and Pt). Co4WPB5 shows an η_{10} and η_{100} values of mere 72 mV and 179 mV which are higher than Pt but are considerably lower than Co4WB (104 mV@10, 227mV@100) and CoPB5 (145 mV@10, 235mV@100). The Tafel slope values of Co4WPB5 (64.1 mV/dec), Co4WB (77.1 mV/dec), and CoPB5 (97.5 mV/dec) indicate Volmer-Heyrovsky mechanism for HER (inset of **Fig. 3a**).[30,47] The Nyquist plots (**Fig. 3b**) obtained from EIS denote a drastic decrease in the R_{ct} for Co4WPB5 (4.7 Ω) when compared to Co4WB (10.6 Ω) and CoPB5 (10.9 Ω), confirming better interfacial charge transfer characteristics in Co4WPB5. Likewise, the calculated C_{DL} values (from CV curves in **Fig. S12a-c**) are much higher for Co4WPB5 (2.3 mF/cm^2) as compared to Co4WB (1.4 mF/cm^2) and CoPB5 (1.8 mF/cm^2) (**Fig. 3c**). On comparing the obtained C_{DL} values and that of a perfectly planar Co surface (0.040 mF/cm^2),[24] the ECSA of Co4WPB5 was calculated to be 57.5 cm^2 which was noticeably higher than Co4WB (34.5 cm^2) and CoPB5 (45.0 cm^2). The highest ECSA value achieved with Co4WPB5 is in agreement with that of the maximum BET surface area. These findings suggest that the inclusion of W and P in optimized amounts leads to higher specific and electrochemical surface area that offers abundant surface-active sites with better interfacial charge transfer properties, eventually leading to lower overpotential.

Following the HER tests, the catalyst compositions of CoWPB were screened for OER (**Fig. S2b, S3b,** and **Table S1**) and interestingly Co4WPB5 did not show good OER activity but alternately, Co2WPB1 was found to be the best configuration. Co2WPB1 displayed remarkable OER activity as it could reach 10 mA/cm^2 and 100 mA/cm^2 at low overpotentials of 262 mV and 370 mV, respectively (**Fig. 3d**). The same current densities were achieved at much higher overpotentials with the reference electrocatalysts of Co2WB (294 mV@10, 429 mV@100) and CoPB1 (310 mV@10, 454 mV@100). It is noteworthy

that the OER activities of Co2WPB1 and both the reference electrocatalysts were significantly better than the traditional benchmark RuO_2[8] that achieved the same current densities at 360 mV@10 and 467 mV@100. Amongst these catalysts, Co2WPB1 portrayed the smallest Tafel slope of 85.6 mV/dec (inset of **Fig. 3d**), which is another indicator of improved reaction kinetics.

OER is a multi-step reaction that proceeds through the formation of oxy-hydroxide intermediates on the catalyst surface [48]. Some of the first-row transition-metals, such as Co and Ni, show redox peaks at potentials lower than the water oxidation potential that indicate the surface reconstruction and formation of OER active sites.[49,50] **Fig. S13** shows the pre-OER oxidation peaks for Co2WPB1 and the two reference samples. During OER, the Co surface is reported to transform from Co^{2+} to Co^{3+} state in the oxidation potentials range of 1.15-1.25 V and from Co^{3+} to Co^{4+} state at slightly higher oxidation potentials (1.29- 1.32 V),[51] providing the most active sites. In the case of Co2WPB1, two distinct oxidation peaks corresponding to these higher oxidation state transformations are observed, whereas the Co2WB and CoPB1 electrocatalysts exhibit a single broad peak (**Fig. S13**). Upon deconvolution of this broad peak, two separate peaks representing these oxidative transformations emerged but with a less pronounced higher oxidation peak in contrast to Co2WPB1 (**Fig. S14** and **Table S3**). The observed oxidation behavior implies that the presence of W and P promotes the formation of active CoOOH species (Co^{3+}) and their conversion to Co^{4+} species on the catalytic surface, facilitating the OER. Co2WPB1 also showed the smallest R_{ct} (7.5 Ω) compared to reference Co2WB (13.9 Ω) and CoPB1 (10.8 Ω) (**Fig. 3e**). The calculated C_{DL} values (from CV curves in **Fig. S12d-f**) were 1.5 mF/cm^2, 1.3 mF/cm^2 and 1.2 mF/cm^2 corresponding to ECSAs of 37.5 cm^2, 32.5 cm^2, and 30.0 cm^2 for Co2WPB1, CoPB1 and Co2WB, respectively (**Fig. 3f**). This is a clear manifestation of the advantage of simultaneous inclusion of W and P that leads to higher number of

electrochemically active surface sites, enhanced charge transfer at interface and generation of active CoOOH sites in Co2WPB1, which eventually translates into higher OER activity.

It must be noted that the HER and OER current densities shown in **Fig. 3a** and **3d** are normalized with respect to the geometric surface area of the working electrode, which remains the same for all samples. To eliminate the contributions from the higher (specific and electrochemical) surface area, all the LSV current values for HER and OER were normalized by the BET surface area (**Fig. S15a, b**) and ECSA (**Fig. S15c, d**). Here, it becomes evident that the HER and OER active catalysts, i.e. Co4WPB5 and Co2WPB1, remain the most active configurations, irrespective of their surface area contributions and hints at their higher catalytic activity per site. To quantify the intrinsic HER and OER activities per catalytic site, turnover frequency (TOF) was calculated for each catalyst,[40] as presented in **Table S4**. For HER, Co4WPB5 (0.0793/atom/s) shows a high TOF value that is almost 1.2 times higher than CoPB5 (0.0663/atom/s) and 2 times higher than Co4WB (0.0403/atom/s). Likewise, for OER, Co2WPB1 (0.0757/atom/s) shows almost 3 times higher TOF value than CoPB1 (0.0244/atom/s) and Co2WB (0.0233/atom/s).

To assess the durability of the optimized HER and OER catalysts, they were subjected to multiple recycling and long-term chronoamperometric tests. Remarkably, after undergoing rigorous tests involving 10,000 cycles of cathodic and anodic recycling, both Co4WPB5 and Co2WPB1 exhibited only marginal declines in their catalytic activities, underscoring their robustness for HER and OER (as illustrated in **Fig. 4a-b**). During the chronoamperometric test (inset of **Fig. 4a**), the HER-active catalyst, Co4WPB5, displayed a slight decrease in current density of 100 mA/cm^2, maintained over a period of 70 h. For the OER catalyst, Co2WPB1 maintained an almost constant current density of 100 mA/cm^2 throughout the entire 70 h test, demonstrating excellent stability for OER (inset of **Fig. 4b**).

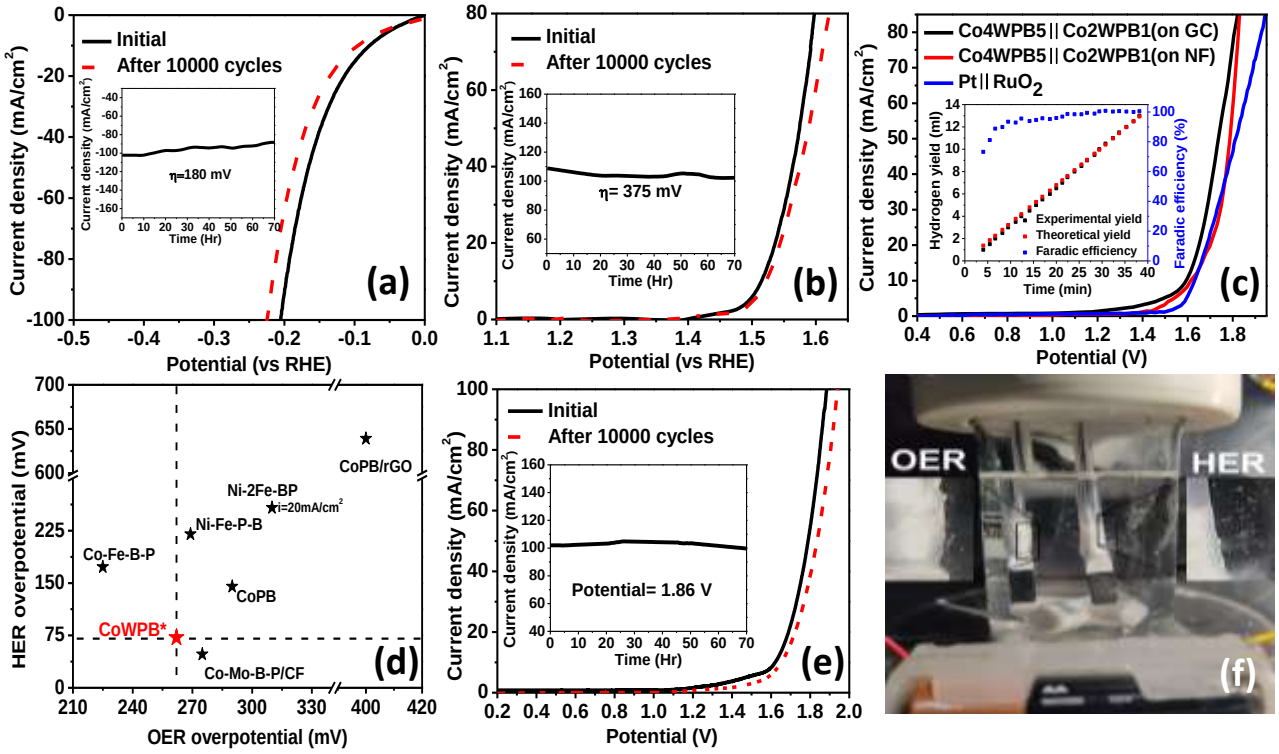

Figure 4: Recycling tests depicting the variation in linear polarization curves for **(a)** HER (Co4WPB5) and **(b)** OER (Co2WPB1) after 10,000 cycles, inset shows the steady-state chronoamperometric tests for 70 h; **(c)** Linear sweep voltammetry in 2-electrode setup for Co4WPB5||Co2WPB1 deposited on glassy carbon (GC) and Ni foam (NF) substrates, along with Pt||RuO_2 assembly, inset shows the theoretical and experimental H_2 yield and the corresponding Faradaic efficiency values for Co4WPB5||Co2WPB1; **(d)** chart comparing the HER and OER activity of CoWPB in terms of overpotential with state of the art bifunctional TMPBs; **(e)** 10,000 recycling test for Co4WPB5||Co2WPB1 on GC, inset shows the chronoamperometric stability test for the same assembly conducted for 70 h at 1.69 V; **(f)** Real image of the 2-electrode setup for Co4WPB5||Co2WPB1 on NF, powered by AA battery and demonstrating H_2 and O_2 gases evolving at the electrodes.

3.1. Overall Water Splitting:

For commercial relevance, it is often desired to establish the electrocatalytic performance of the catalysts in two-electrode assemblies.[2] Owing to the bifunctionality of CoWPB, both the HER-active and the OER-active configurations were used to construct the cathode and anode over GC electrode, respectively, denoted as Co4WPB5||Co2WPB1. As reference data, the traditional HER and OER benchmarks of Pt and RuO_2 (Pt||RuO_2) were also used as another set of electrodes. The Co4WPB5||Co2WPB1 assembly required a small potential of 1.59 V to achieve the current density of 10 mA/cm^2 which is 40 mV less than the Pt||RuO_2 assembly (1.63 V) **(Fig. 4c)**. As commercial alkaline water electrolyzers use Ni foam as catalyst supports, both the catalysts were coated on Ni foam substrate as well for comparison, keeping the catalyst loading constant. The Co4WPB5||Co2WPB1 assembly deposited on Ni-foam required a potential of 1.61 V to achieve the current density of 10 mA/cm^2 **(Fig. 4c)** which shows that the activity of electrocatalysts loaded on GC and NF is similar. It is noteworthy that at higher current densities (>40 mA/cm^2), Co4WPB5||Co2WPB1 assembly outclasses the Pt||RuO_2 assembly, establishing its superior performance over the noble metal catalysts. To ascertain that the produced current is due to hydrogen and oxygen evolution reactions, the gases evolved during the two-electrode measurements (for Co4WPB5||Co2WPB1) were quantified and matched with the theoretically expected volumes, yielding a Faradaic efficiency ~100% (inset of **Fig. 4c**). Moreover, the observed performance in 2-electrode assembly supersedes the reported transition metal phospho-boride electrocatalysts in 1 M KOH, as represented in **Fig. 4d** as well as **Table S7**. Additionally, the Co4WPB5||Co2WPB1 assembly, designed for overall water splitting, exhibited only marginal decline in activity after undergoing 10,000 cycles of recycling (**Fig. 4e**) and a 70 h chronoamperometric test at 100 mA/cm^2 (inset of **Fig. 4e**).

Fig. 4f and **Video S1** demonstrates a 2-electrode cell created with Co4WPB5||Co2WPB1 assembly and powered by a single AA battery (1.5 V). A copious amount of hydrogen and oxygen bubbles can be seen on both electrodes, demonstrating the practical relevance of the bifunctional CoWPB catalyst.

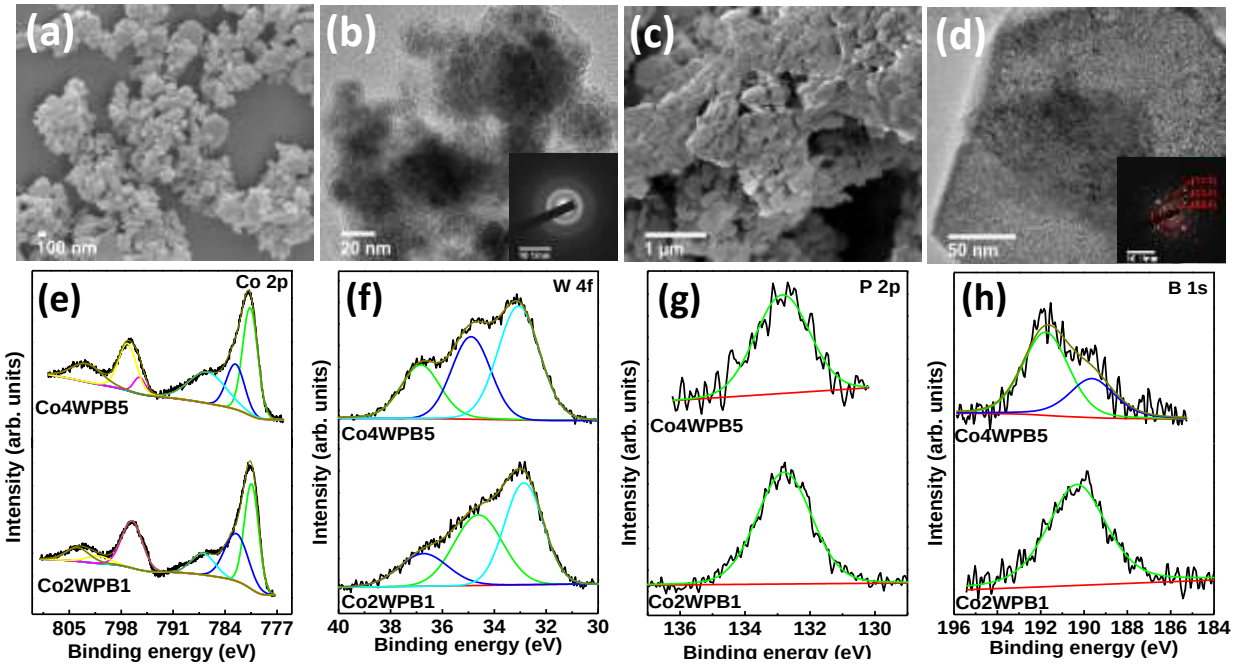

Figure 5: (a) SEM and **(b)** TEM image of Co4WPB5 after HER test; **(b)** SEM and **(d)** TEM image of Co2WPB1 after OER test, inset images in **(b)** and **(d)** are the diffraction patterns corresponding to the TEM image; High-resolution XPS spectra for **(e)** Co 2p, **(f)** W 4f, **(g)** P 2p and **(h)** B 1s levels in Co4WPB5 post HER (upper panels) and Co2WPB1 post OER (lower panels).

3.2. Post-Electrochemical reaction characterization:

To observe the morphological change in the catalysts after electrochemical measurements, SEM and TEM images were obtained for the catalyst powder collected after HER and OER tests (1-hour chronoamperometric test). Co4WPB5 could maintain its amorphous nanoparticle-like morphology with relatively smaller size of the particles and higher

coalescence (**Fig. 5a, b**). On the other hand, Co2WPB1 shows a drastic transformation from large flake-like morphology to smaller agglomerated flakes (**Fig. 5c, d**). In addition to this, the amorphous Co2WPB1 structure crystallizes into active CoOOH, as evident from the diffraction spots in SAED pattern corresponding to an interplanar spacing of 0.45 nm, 0.24 nm and 0.15nm of (003), (012), (110) planes respectively (inset of **Fig. 5d**).[52] The intrinsic change in the catalyst surface during the electrochemical activity was examined by determining the C_{DL} values (from CV curves in **Fig. S16a-d**) and hence the ECSA. After HER test, a huge increase in C_{DL} can be observed for Co4WPB5, resulting in 5.3 times increase in the ECSA from 57.5 cm^2 to 307.5 cm^2 (**Fig. S17a**). This drastic increase in the ECSA confirms the surface modification conducive for HER by generating surface-active sites for H-adsorption. After OER, the C_{DL} value of Co2WPB1 increases marginally (**Fig. S17b**) which can be directly related to the agglomeration of nanoflakes that hinders surface-to-volume ratio. Despite this setback, the OER activity and stability in Co2WPB1 are substantially high owing to the formation of CoOOH active sites.

To understand the change in the surface chemical states after electrochemical reactions, XPS was performed by collecting the electrocatalysts after HER and OER. In Co4WPB5, $Co2p_{3/2}$ spectra (**Fig. 5e, upper panel**) show the presence of two peaks at BE of 781.0 eV and 782.6 eV corresponding to oxidized cobalt. A satellite peak at 786.4 eV was also observed, followed by peaks of the $Co2p_{1/2}$ state. Deconvoluted W 4f spectra (**Fig. 5f, upper panel**) revealed the formation of the metallic peak at 33.1 eV[22] along with oxidized forms at BE of 34.9 eV and 36.8 eV. P 2p spectra (**Fig. 5g, upper panel**) showed only oxidized phosphorous at BE of 132.8 eV and B1s spectra (**Fig. 5h, upper panel**) revealed oxidized boron at BE of 189.6 eV and 191.8 eV. In Co2WPB1, Co $2p_{3/2}$ spectra (**Fig. 5e, lower panel**) depict a peak at BE of 780.4 eV assigned to active CoOOH type species[8] along with a corresponding satellite peak at 786.9 eV. Similar peaks were observed in the $Co2p_{1/2}$ spectra.

W 4f spectra (**Fig. 5f, lower panel**) showed metallic (32.9 eV) as well as oxidized tungsten (34.6 eV and 36.7 eV). Both P 2p (**Fig. 5g, lower panel**) and B 1s (**Fig. 5h, lower panel**) spectra exhibit oxidized phosphorous (132.8 eV) and boron (190.3 eV) respectively. This suggests that all three elements (Co, P, and B) lose their metallic nature, while W which was in an oxidized state initially appears in metallic form after both half-reactions.

4. Computational analysis

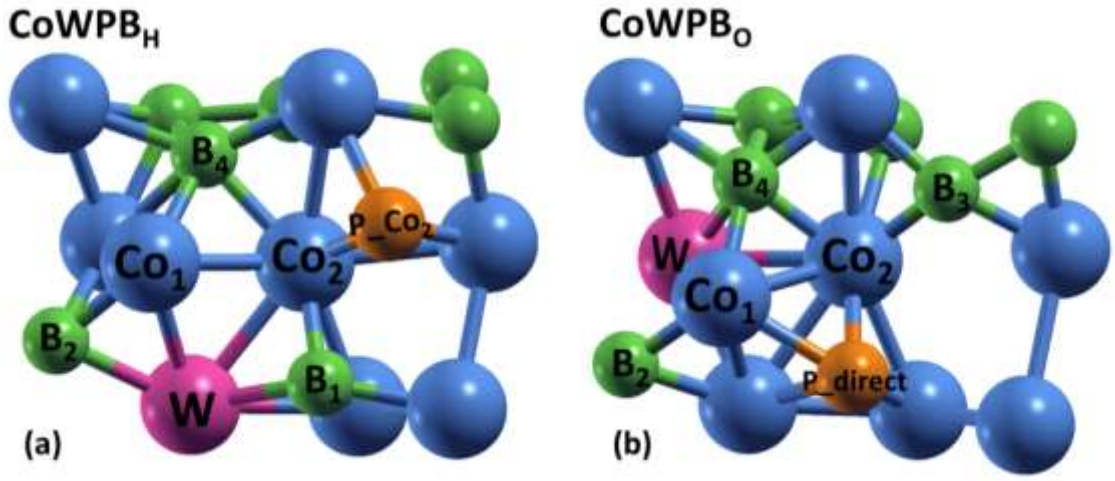

Figure 6: Top view of a few layers shown of amorphous Co-WP-B with **(a)** P_Co_2 and **(b)** P_direct [Co, B, W, and P atoms are shown with atoms in blue, green, pink, and orange color, respectively]

To further investigate the reaction mechanism and the specific roles played by each element in CoWPB, computational investigation was performed using DFT. For this study, CoWB was used as the base model to incorporate P and construct CoWPB cluster. In our past study, detailed understanding was developed for enhancement of HER and OER due to W incorporation[22] in amorphous Co-B, revealing presence of multi-catalytic and selective sites. It was discovered that the W atom interacting with single Co atom (W@Co) and both

Co and B atoms (W@Co/B) displayed good OER and HER activity, respectively, which is designated as $CoWB_O$ and $CoWB_H$ in the present study. The four different B atoms around these HER and OER active sites of CoWB were selected to insert the P atom resulting in eight different models as detailed in the methodology section. Details regarding each configuration and its nomenclature are given in **Fig. S1** and **Table S5**. The overpotential values calculated for HER and OER over Co and P sites in these eight models are summarized in **Table S5**. Among all eight models, two distinct cases, i.e., P_Co_2_Co-WP-B and P_direct_Co-WP-B exhibit the lowest overpotential values of 0.015V and 0.731V for HER and OER respectively. Hereon, both these suitable models of CoWPB for HER and OER are termed $CoWPB_H$ (**Fig. 6a**) and $CoWPB_O$ (**Fig. 6b**), respectively, and considered for further studies. To analyze the role of W and P in governing the enhancement of catalytic activity on simultaneous incorporation, specific configurations containing W and P are discussed against their counterparts (CoB, CoWB, and CoPB) containing either W or P only with similar nomenclature.

The reaction free energies were calculated for the two optimal configurations and compared with the reference models of CoB, CoPB, and CoWB. The calculated Gibbs free energy (ΔG) for HER (**Fig. 7a**) clearly indicates that $CoWPB_H$ has a ΔG value close to zero (-0.015 eV), which is representative of the optimal H-bonding strength and explains its superior HER kinetics. CoB shows the worst ΔG value, which improves when W or P are incorporated individually but the best result is obtained by concomitant inclusion of both W and P, as in $CoWPB_H$, which is directly translated into the lowest overpotential (**Table 1**). For OER, the Gibbs free energy diagrams (**Fig. 7b-d**) denote $^*O$ to $^*OOH$ formation as the rate-limiting step in Co-WP-B_O as well as the reference models, at all applied potentials. Gibbs free energy of $^*OH$ and *OOH follows universal scaling relation with constant difference ~ 3.2 ± 0.2 eV,[53,54] while enhancement in OER activity requires ideally ΔG_O of

about $(\Delta G_{OOH} + \Delta G_{OH})/2$. ΔG_O in $CoWPB_O$ shows lowest deviation from its ideal ΔG_O value resulting in lowest overpotential for OER. The calculated OER overpotentials (**Table 1**) confirm that $CoWPB_O$ shows the best OER activity, in accordance with the experimental results.

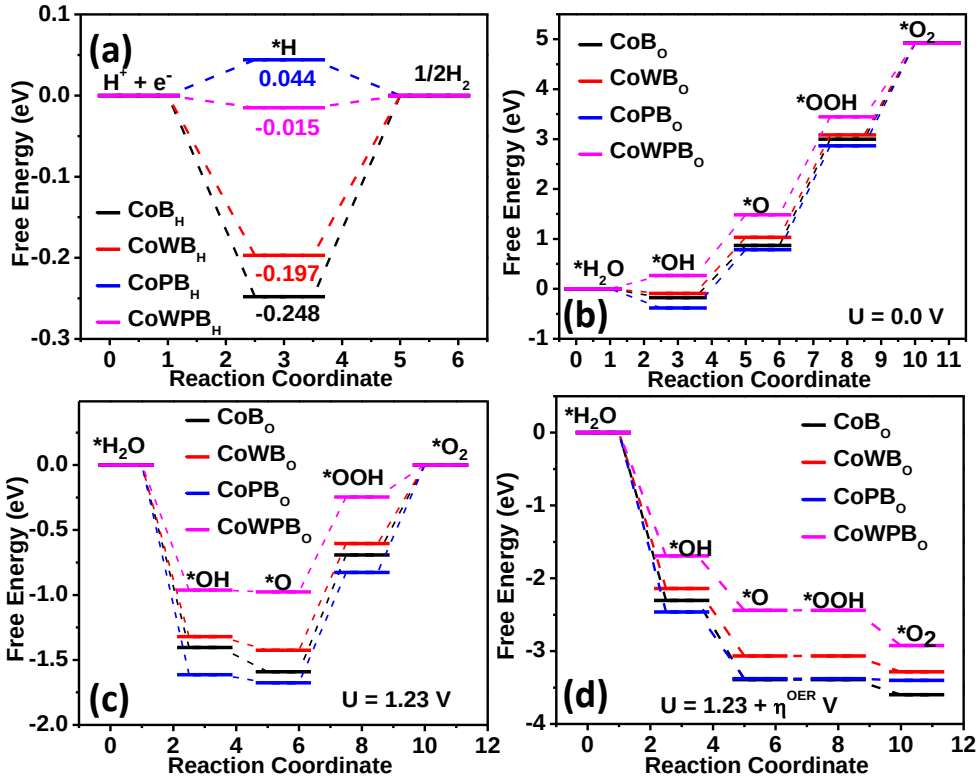

Figure 7: (a) Gibbs free energy for HER at potential U=0 and for OER at potential **(b)** U = 0.0, **(c)** U = 1.23, and **(d)** U = 1.23 + η^{OER} for pristine amorphous CoB, CoWB, CoPB, and CoWPB cluster (Nomenclature follows **Table 1** for respective adsorption configurations).

DOS plot provides information about the orbital interaction along with the activation of the atoms in terms of the orbital intensity variation over the surface atoms. DOS, partial DOS (PDOS), and orbital DOS (ODOS) are plotted (**Fig. 8a and S18**) for Co-WP-B_H and Co-WP-B_O, with Fermi energies (E_F) of 3.248 and 3.253 eV, respectively. Metallic characteristics can be seen for both configurations, although the substitution of P and its

interaction with the nearest atom governs the occupation of states around the Fermi level. The observed peak shift in PDOS (**Fig. 8a**) for Co_1-3d is due to its orbital overlap with the W-atom, while the shoulder intensity variation is a result of Co-3d_{z^2}, Co-3$d_{x^2-y^2}$ orbital interaction with the respective orbitals of W (**Fig. S18**).

Table 1: Comparative change in Gibbs free energy for rate determining step and overpotential for HER and OER over different amorphous systems.

Model		**HER**		**OER**		**HER/OER active site**
		ΔG_{H^*}**(eV)**	η_{HER}**(V)**	ΔG**(eV)**	η_{OER}**(V)**	
Co-B		-0.248	0.248	--	--	Over B
		--	--	2.130[3#]	0.900	Over Co_1
Co-W-B	**$CoWB_H$**	-0.197	0.197	2.547[4#]	1.317	Over Co_1-B_1 bond
	$CoWB_O$	-0.493	0.493	2.051[3#]	0.821	Over Co_1
Co-P-B	**$CoPB_H$**	-0.088	0.088	--	--	Over P
	$CoPB_O$	-0.452	0.452	2.080[3#]	0.850	Over Co_1
Co-WP-B	**$CoWPB_H$**	-0.015	0.015	--	--	Over P
	$CoWPB_O$	--	--	1.961[3#]	0.731	Over Co_1

† n# is rate determining step ΔG_n;

For OER n#⇒ 1: $H_2O \rightarrow OH$, 2: $OH \rightarrow O$, 3: $O \rightarrow OOH$, 4: $OOH \rightarrow O_2$

Here, the interaction of Co_{3d}-W_{5d} orbitals with direct, indirect bonding creates a charge conjugation within the system and the charge variation is due to the change in Mulliken electronegativity[55] of the corresponding atoms. This difference along with the electron affinity of the surface atoms may influence an electron to transfer over the catalyst surface and contribute towards the redox activity. Electron localization function (ELF) plots were obtained by plotting the surface Co, B, and P atoms in their corresponding plane contour form to study the electron localization and bonding nature over the surface atoms (**Fig. 8 b,c**).

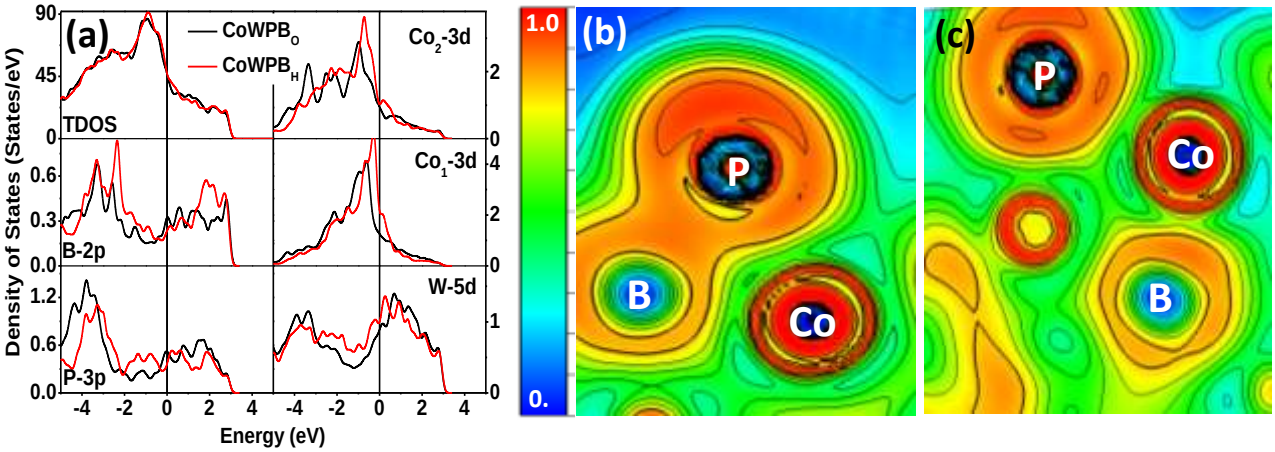

Figure 8: (a) Total and partial DOS for $CoWPB_O$ and $CoWPB_H$, Electron localization function for **(b)** $CoWPB_H$ and **(c)** $CoWPB_O$ configuration.

On the ELF scale, red indicates regions having high electron localization such as covalent bonding while blue represents ionic nature and the central green region denotes metallic bonding. In $CoWPB_H$ (**Fig. 8b**), electron localization gradient is seen between Co and B, and Co and P atoms suggest metallic bonding between these atoms, whereas P and B atoms show covalent-type bonding. The highest charge region is observed around the P atom (red region) as a result of its lone pair, which suggests it to be a favorable site for HER. In the $CoWPB_O$ model (**Fig. 8c**), the covalent bonding between P and B atoms was missing due to their large separation unlike in the previous case. Alternately, the reduced charge gradient

between the Co-B atoms showcases charge conjugation over the Co-B bond. The optimized electron density over the Co atom would make it more favorable for initiating OER.

Fig. 9 represents the charge density difference Δρ for HER and OER over the two favorable sites, where $\Delta\rho = \rho^{system} - (\rho^{Adsorbent} + \rho^{Adsorbate})$. For HER, the H-atom is adsorbed over the favorable P-atom, where Δρ over the surface is clearly observed in **Fig. 9**. Δρ around P-H bonding shows depletion region, while e^- accumulation is seen between the P-Co bonding for neighboring Co-atom.

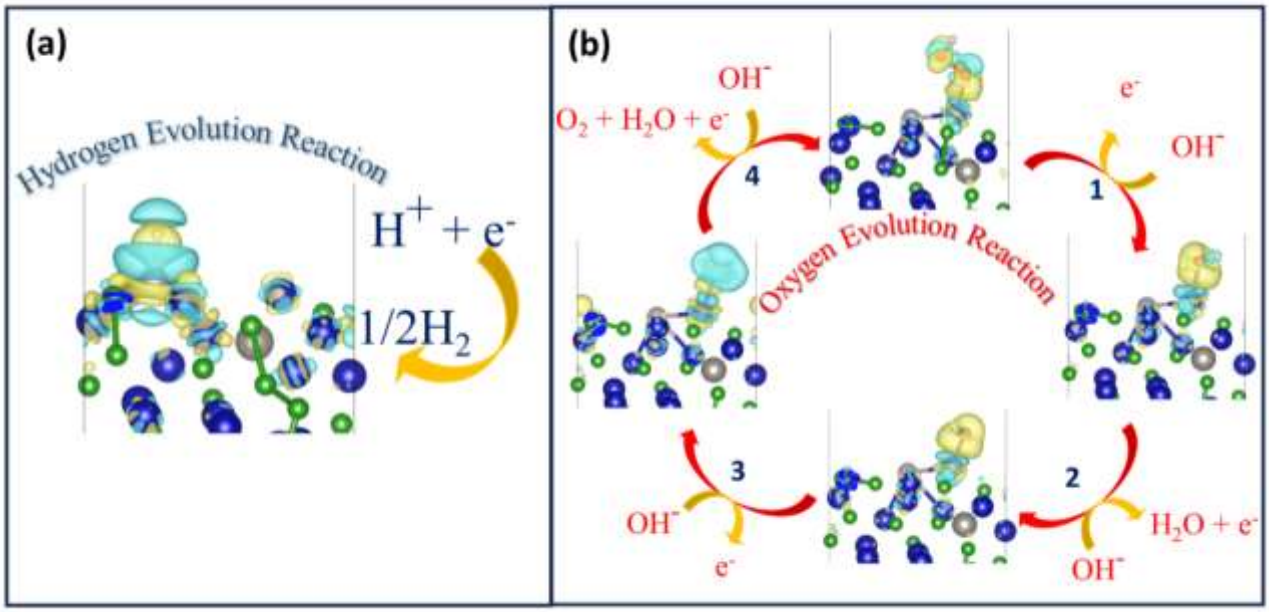

Figure 9: Charge density difference for **(a)** HER ($CoWPB_H$), and **(b)** OER ($CoWPB_O$), where yellow (blue) region denotes accumulation (depletion) of electron. Blue, Green, Grey, Plum, and White balls respectively represent Cobalt, Boron, Tungsten, Phosphorus, and Hydrogen atom.

In case of OER, H_2O molecule adsorption is seen over the Co-atom, as predicted from ELF plots. An e^- depletion is observed over the Co-O and O-H bonds while e^- accumulation takes place over O and Co atoms. For the next OER step, where $^*OH$ is formed over the surface, e^- accumulation over O intensifies with e^- depletion is seen over the Co-atom.

Similar findings are observed for the third OER step involving $^{*}O$. At the 4th step, addition of another water molecule forms $^{*}OOH$, where accumulation is seen over O atom while depletion over O-H bond and the charge redistribution over the surface atoms enhances the surface adsorption.

Löwdin charge values over each surface atom is represented in **Table S~~5~~6**, for CoWPB as well as the reference configurations of CoB, CoPB and CoWB for both HER and OER models. In CoB, B and Co atoms from TF-2CoB site are active centers for HER and OER, respectively. The charges over Co and B atoms in CoB will be taken as reference to understand the charge transfer behavior. For HER active site in $CoWB_H$, charges over Co_1, B_1, B_2, and B_4 atoms decrease, suggesting that the W atom acts as a charge accumulator and changes the bonding characteristics of Co_1-B_1 from metallic to ionic[22] enhancing HER activity over Co_1-B_1 bond. In $CoPB_H$, P atom acts as an active site for HER due to charge accumulation. When both W and P are present together, as in $CoWPB_H$, there is a redistribution of charges across all atoms showing slightly more charge accumulation over the P atom and slightly less charge accumulation by the W atom. This synergistic role played by W and P creates a delicate charge balance optimizing the binding of adsorbed H over the P atom. For OER activity, the Co_1 atom remains an active site for all amorphous cases, but significant improvement in overpotential is observed after the incorporation of W and P due to improvement in the binding of reaction intermediates over the Co_1 atom. In OER active sites, the P atom shows more charge accumulation than observed in HER active sites. This altered charge distribution over the P atom along with the W atom leads to an increment in Gibbs free energy of $^{*}OH$, $^{*}O$ and $^{*}OOH$ reaction intermediates at 0 V as observed in **Fig. 7b** along with satisfying scaling relations. In $CoWB_O$, charge transfer occurs from Co and B to W atom. Conversely, in $CoPB_O$, P atom leads to charge transfer from interior bulk region to surface active site increasing charges over Co_1, B and P atoms. Incorporation of

both W and P ($CoWPB_O$), shows combined effects of charge redistribution caused by W and charge accumulation to surface by P leading to enhanced OER activity.

Based on the computational analyses, it is now clear that the HER and OER take place over two different types of sites, offered by two different configurations of CoWPB, as also reflected in the experimental data. The synergistic role played by both W and P leads the TF-2CoB site to enhance either HER activity or OER activity in CoWPB by altering the binding strength of reactant species. For HER, the P atom acts as the active site in $CoWPB_H$ while the Co site is found to be the active one for OER. These observations are firmly supported by computational data and match well with the experimental observations, providing a better insight of such complex multi-component amorphous systems. In summary, each element in the catalyst serves a distinct function in enhancing the activity for both the HER and the OER. P and Co act as active centers[17,22,40,56] for HER and OER, particularly in the presence of other elements. On the other hand, tungsten (W) serves to prevent agglomeration, thereby increasing the available surface area with a larger number of active sites, consequently leading to an expansion in the BET surface area and ECSA.

5. Conclusion

To conclude, amorphous CoWPB was discovered as a new member of the fast-growing phospho-boride family of bifunctional electrocatalysts for overall water-splitting. The catalyst was optimized by varying the molar ratio of W/(W+Co) and that of B/P. Co4WPB5 and Co2WPB1 with B/P ratios of 5 and 1 were the most active for HER (η_{10} = 72 mV) and OER (η_{10} = 262 mV), respectively, compared to the reference electrocatalysts. Moreover, a 2-electrode assembly fabricated using Co4WPB5 and Co2WPB1 yielded a much lower cell potential (1.59 V at 10 mA/cm^2) with good stability (70 h) and excellent recyclability (10000 cycles). While exploring the role of each element, nanoparticles were observed for

Co4WPB5 with low P concentration, while nanoflakes were evident for Co2WPB1 with equal amounts of P and B, implying that the morphology was dictated by the metalloids. The presence of W led to enhancement in both physical and electrochemical surface area, while electron modulation within the elements was attributed to the cooperative influence of B and P. In agreement with experimental results, the computational analyses also depict the presence of two distinct types of sites that are conducive for HER and OER, with the optimum ΔG obtained with the inclusion of both W and P in the Co-B cluster. The distribution of electronic charges across the surface atoms within CoWPB, as well as the behavior of charge transfer during both the HER and the OER, revealed that the P-sites exhibit the highest activity for HER, while the Co-sites are well-suited for OER. A good correlation between the experimental and computational results presented a new understanding of the reaction mechanism in such complex amorphous systems. We believe that this work will be the starting point of discovering more of such novel multi-component amorphous systems and gaining new knowledge that will eventually lead to unprecedented material activities.

Declaration of competing interest

The authors declare that they have no known competing financial interests or personal relationships that could have appeared to influence the work reported in this paper.

Acknowledgements

A. Bhide and M. Patel acknowledges the research grant from UK Commonwealth Commission through Commonwealth Split-Site Fellowship (INCN-2021-45). N. Patel and R. Fernandes thank the Department of Science and Technology (DST), Ministry of Science and Technology, India for providing funds under the AHFC project (DST/TMD-

EWO/AHFC-2021/100), Indo-Italian Project (INT/Italy/P-42/2022(ER)(G)) and FIST program (SR/FST/PS-I/2022/208). N. Patel would like to acknowledge the Board of Nuclear Sciences, DAE, India to fund the project (51/14/03/2023-BRNS/11376). N. Patel and R. Fernandes thank CHRIST (Deemed to be University) for providing SEED funding (SMSS-2107/2108). A. Dashora is grateful to UGC, New Delhi for the Assistant Professorship under the Faculty Recharge Program. A. Dashora would also like to acknowledge the National Supercomputing Mission (NSM) for providing computing resources of 'PARAM Ananta' at IIT Gandhinagar. S. Gupta acknowledges the Project Borocat (J2-50055) funded by the Slovenian Research and Innovation Agency.

Appendix A. Supplementary data

References

(1) Momirlan, M.; Veziroglu, T. N. Current Status of Hydrogen Energy. *Renewable and Sustainable Energy Reviews*. 2002, pp 141–179. https://doi.org/10.1016/S1364-0321(02)00004-7.

(2) Yue, M.; Lambert, H.; Pahon, E.; Roche, R.; Jemei, S.; Hissel, D. Hydrogen Energy Systems: A Critical Review of Technologies, Applications, Trends and Challenges. *Renewable and Sustainable Energy Reviews*. Elsevier Ltd 2021, p 111180. https://doi.org/10.1016/j.rser.2021.111180.

(3) Ramachandran, R.; Menon, R. K. An Overview of Industrial Uses of Hydrogen. *International Journal of Hydrogen Energy*. 1998, pp 593–598. https://doi.org/10.1016/s0360-3199(97)00112-2.

(4) Ausfelder, F.; Bazzanella, A. Hydrogen in the Chemical Industry. In *Hydrogen Science and Engineering: Materials, Processes, Systems and Technology*; 2016; Vol. 1, pp 19–39. https://doi.org/10.1002/9783527674268.ch02.

(5) Liu, W.; Zuo, H.; Wang, J.; Xue, Q.; Ren, B.; Yang, F. The Production and Application of Hydrogen in Steel Industry. *International Journal of Hydrogen Energy*. Elsevier Ltd 2021, pp 10548–10569. https://doi.org/10.1016/j.ijhydene.2020.12.123.

(6) You, B.; Sun, Y. Innovative Strategies for Electrocatalytic Water Splitting. *Acc. Chem. Res.* **2018**, *51* (7), 1571–1580. https://doi.org/10.1021/acs.accounts.8b00002.

(7) Du, N.; Roy, C.; Peach, R.; Turnbull, M.; Thiele, S.; Bock, C. Anion-Exchange Membrane Water Electrolyzers. *Chemical Reviews*. 2022, pp 11830–11895. https://doi.org/10.1021/acs.chemrev.1c00854.

(8) Chunduri, A.; Gupta, S.; Bapat, O.; Bhide, A.; Fernandes, R.; Patel, M. K.; Bambole, V.; Miotello, A.; Patel, N. A Unique Amorphous Cobalt-Phosphide-Boride Bifunctional Electrocatalyst for Enhanced Alkaline Water-Splitting. *Appl. Catal. B Environ.* **2019**, *259* (July), 118051. https://doi.org/10.1016/j.apcatb.2019.118051.

(9) Wang, X.; He, Q.; Ge, Q.; Fu, T.; Chen, S.; Zhou, P.; Xiao, F.; He, P.; Jia, L.; Jia, B.; Zhang, H.; Pan, K.; Liu, H. Self-Assembled Nanocotton-like Co–B–P/Bacterial Cellulose Based Carbon Nanofiber as Highly Efficient Electrocatalyst for Oxygen Evolution Reaction. *Int. J. Hydrogen Energy* **2021**, *46* (40), 20930–20940. https://doi.org/10.1016/j.ijhydene.2021.03.211.

(10) Li, P.; Jin, Z.; Xiao, D. A One-Step Synthesis of Co-P-B/RGO at Room Temperature with Synergistically Enhanced Electrocatalytic Activity in Neutral Solution. *J. Mater.*

Chem. A **2014**, *2* (43), 18420–18427. https://doi.org/10.1039/c4ta03962a.

(11) Yu, N.; Ma, Y.; Ren, J. K.; Zhang, Z. J.; Liu, H. J.; Nan, J.; Li, Y. C.; Chai, Y. M.; Dong, B. High Negative Voltage Activating Perovskite Oxide with Bi-Vacancy Synergistic Regulation for Water Oxidation. *Chem. Eng. J.* **2023**, *478* (August). https://doi.org/10.1016/j.cej.2023.147415.

(12) Xie, J. Y.; Liu, Z. Z.; Li, J.; Feng, L.; Yang, M.; Ma, Y.; Liu, D. P.; Wang, L.; Chai, Y. M.; Dong, B. Fe-Doped CoP Core–Shell Structure with Open Cages as Efficient Electrocatalyst for Oxygen Evolution. *J. Energy Chem.* **2020**, *48*, 328–333. https://doi.org/10.1016/j.jechem.2020.02.031.

(13) Zhang, X.; Feng, C.; Dong, B.; Liu, C.; Chai, Y. High-Voltage-Enabled Stable Cobalt Species Deposition on MnO2 for Water Oxidation in Acid. *Adv. Mater.* **2023**, *35* (13), 1–12. https://doi.org/10.1002/adma.202207066.

(14) Gong, L.; Lan, K.; Wang, X.; Huang, X.; Jiang, P.; Wang, K.; Yang, M.; Ma, L.; Li, R. Carbon-Coated Co-Mo-P Nanosheets Supported on Carbon Cloth as Efficient Electrocatalyst for Hydrogen Evolution Reaction. *Int. J. Hydrogen Energy* **2020**, *45* (1), 544–552. https://doi.org/10.1016/j.ijhydene.2019.10.248.

(15) Jiao, M.; Chen, Z.; Zhang, X.; Mou, K.; Liu, L. Multicomponent N Doped Graphene Coating Co@Zn Heterostructures Electrocatalysts as High Efficiency HER Electrocatalyst in Alkaline Electrolyte. *Int. J. Hydrogen Energy* **2020**, *45* (33), 16326–16336. https://doi.org/10.1016/j.ijhydene.2020.04.121.

(16) Xie, Y.; Liu, Y.; Yang, Z. Interfaces Engineering of MoNi-Based Sulfides Electrocatalysts for Hydrogen Evolution Reaction in Both Acid and Alkaline Media. *Int. J. Hydrogen Energy* **2020**, *45* (11), 6500–6507.

https://doi.org/10.1016/j.ijhydene.2019.12.181.

(17) Gupta, S.; Patel, N.; Miotello, A.; Kothari, D. C. Cobalt-Boride: An Efficient and Robust Electrocatalyst for Hydrogen Evolution Reaction. *J. Power Sources* **2015**, *279*, 620–625. https://doi.org/10.1016/j.jpowsour.2015.01.009.

(18) Silviya, R.; Vernekar, Y.; Bhide, A.; Gupta, S.; Patel, N.; Fernandes, R. Non-Noble Bifunctional Amorphous Metal Boride Electrocatalysts for Selective Seawater Electrolysis. *ChemCatChem* **2023**, *15* (17). https://doi.org/10.1002/cctc.202300635.

(19) Yang, L.; Guo, Z.; Huang, J.; Xi, Y.; Gao, R.; Su, G.; Wang, W.; Cao, L.; Dong, B. Vertical Growth of 2D Amorphous FePO4 Nanosheet on Ni Foam: Outer and Inner Structural Design for Superior Water Splitting. *Adv. Mater.* **2017**, *29* (46), 1–9. https://doi.org/10.1002/adma.201704574.

(20) Tran, P. D.; Tran, T. V.; Orio, M.; Torelli, S.; Truong, Q. D.; Nayuki, K.; Sasaki, Y.; Chiam, S. Y.; Yi, R.; Honma, I.; Barber, J.; Artero, V. Coordination Polymer Structure and Revisited Hydrogen Evolution Catalytic Mechanism for Amorphous Molybdenum Sulfide. *Nat. Mater.* **2016**, *15* (6), 640–646. https://doi.org/10.1038/nmat4588.

(21) Liu, W.; Liu, H.; Dang, L.; Zhang, H.; Wu, X.; Yang, B.; Li, Z.; Zhang, X.; Lei, L.; Jin, S. Amorphous Cobalt–Iron Hydroxide Nanosheet Electrocatalyst for Efficient Electrochemical and Photo-Electrochemical Oxygen Evolution. *Adv. Funct. Mater.* **2017**, *27* (14). https://doi.org/10.1002/adfm.201603904.

(22) Chunduri, A.; Bhide, A.; Gupta, S.; Mali, K. H.; Bhagat, B. R.; Dashora, A.; Spreitzer, M.; Fernandes, R.; Patel, R.; Patel, N. Exploring the Role of Multi-Catalytic Sites in an Amorphous Co-W-B Electrocatalyst for Hydrogen and Oxygen Evolution

Reactions. *ACS Appl. Energy Mater.* **2023**, *6* (9), 4630–4641. https://doi.org/10.1021/acsaem.2c04164.

(23) Chunduri, A.; Gupta, S.; Patel, M.; Forster, M.; Cowan, A. J.; Patel, N. Alkaline Water Oxidation Using a Bimetallic Phospho-Boride Electrocatalyst. *ChemSusChem* **2020**, *13* (24), 6534–6540. https://doi.org/10.1002/cssc.202002269.

(24) Chen, Z.; Zheng, R.; Graś, M.; Wei, W.; Lota, G.; Chen, H.; Ni, B. J. Tuning Electronic Property and Surface Reconstruction of Amorphous Iron Borides via W-P Co-Doping for Highly Efficient Oxygen Evolution. *Appl. Catal. B Environ.* **2021**, *288* (January). https://doi.org/10.1016/j.apcatb.2021.120037.

(25) Liu, X.; He, G.; Liu, H.; Zhu, Y.; Xiao, J.; Han, L. Boron-Doped Cobalt-Iron Bimetal Phosphides Nanosheets for Enhanced Oxygen Evolution. *J. Alloys Compd.* **2022**, *893*, 162208. https://doi.org/10.1016/j.jallcom.2021.162208.

(26) Wang, D.; Deng, Y. P.; Zhang, Y.; Zhao, Y.; Zhou, G.; Shui, L.; Hu, Y.; Shakouri, M.; Wang, X.; Chen, Z. Defect Engineering on Three-Dimensionally Ordered Macroporous Phosphorus Doped Co3O4–δ Microspheres as an Efficient Bifunctional Electrocatalyst for Zn-Air Batteries. *Energy Storage Mater.* **2021**, *41* (June), 427–435. https://doi.org/10.1016/j.ensm.2021.06.017.

(27) Wang, F. G.; Liu, X.; Yuan, X. Q.; Wu, Y.; Zhao, H. Y.; Yu, J. F.; Liu, B.; Chai, Y. M.; Dong, B. Constructing Porous Boron Doped Nickel Phosphide (Ni2P) Rod Arrays with Optimized Electron Coordination for Alkaline Hydrogen Evolution. *J. Alloys Compd.* **2022**, *927*, 166938. https://doi.org/10.1016/j.jallcom.2022.166938.

(28) Ren, H.; Sun, X.; Du, C.; Zhao, J.; Liu, D.; Fang, W.; Kumar, S.; Chua, R.; Meng, S.; Kidkhunthod, P.; Song, L.; Li, S.; Madhavi, S.; Yan, Q. Amorphous Fe-Ni-P-B-O

Nanocages as Efficient Electrocatalysts for Oxygen Evolution Reaction. *ACS Nano* **2019**, *13* (11), 12969–12979. https://doi.org/10.1021/acsnano.9b05571.

(29) Ma, X.; Zhang, S.; He, Y.; He, T.; Li, H.; Zhang, Y.; Chen, J. Boron and Phosphorus Co-Doped NiVFe LDHs@NF as a Highly Efficient Self-Supporting Electrocatalyst for the Hydrogen Evolution Reaction. *J. Electroanal. Chem.* **2021**, *886* (November 2020). https://doi.org/10.1016/j.jelechem.2021.115107.

(30) Wu, Z.; Nie, D.; Song, M.; Jiao, T.; Fu, G.; Liu, X. Facile Synthesis of Co-Fe-B-P Nanochains as an Efficient Bifunctional Electrocatalyst for Overall Water-Splitting. *Nanoscale* **2019**, *11* (15), 7506–7512. https://doi.org/10.1039/c9nr01794a.

(31) Wei, Y.; Zou, P.; Yue, Y.; Wang, M.; Fu, W.; Si, S.; Wei, L.; Zhao, X.; Hu, G.; Xin, H. L. One-Pot Synthesis of B/P-Codoped Co-Mo Dual-Nanowafer Electrocatalysts for Overall Water Splitting. *ACS Appl. Mater. Interfaces* **2021**, *13* (17), 20024–20033. https://doi.org/10.1021/acsami.1c01341.

(32) Deng, X.; Zhang, R.; Li, Q.; Gu, W.; Hao, L. Bimetallic Boron Phosphide Ni-2Fe-BP as an Active Water-Splitting Catalyst. *ChemistrySelect* **2022**, *7* (21). https://doi.org/10.1002/slct.202200091.

(33) Tang, W.; Liu, X.; Li, Y.; Pu, Y.; Lu, Y.; Song, Z.; Wang, Q.; Yu, R.; Shui, J. Boosting Electrocatalytic Water Splitting via Metal-Metalloid Combined Modulation in Quaternary Ni-Fe-P-B Amorphous Compound. *Nano Res.* **2020**, *13* (2), 447–454. https://doi.org/10.1007/s12274-020-2627-x.

(34) Ali, M. An Inclusive Perspective on the Recent Development of Tungsten-Based Catalysts for Overall Water-Splitting : A Review. **2022**, No. January, 10228–10258. https://doi.org/10.1002/er.7800.

(35) Fernandes, R.; Patel, N.; Paris, A.; Calliari, L.; Miotello, A. Improved H2 Production Rate by Hydrolysis of Ammonia Borane Using Quaternary Alloy Catalysts. *Int. J. Hydrogen Energy* **2013**, *38* (8), 3313–3322. https://doi.org/10.1016/j.ijhydene.2012.12.085.

(36) Patel, N.; Fernandes, R.; Miotello, A. Promoting Effect of Transition Metal-Doped Co-B Alloy Catalysts for Hydrogen Production by Hydrolysis of Alkaline NaBH4 Solution. *J. Catal.* **2010**, *271* (2), 315–324. https://doi.org/10.1016/j.jcat.2010.02.014.

(37) Zhang, J.; Zhou, Y.; Zhang, S.; Li, S.; Hu, Q.; Wang, L.; Wang, L.; Ma, F. Electrochemical Preparation and Post-Treatment of Composite Porous Foam NiZn Alloy Electrodes with High Activity for Hydrogen Evolution. *Sci. Rep.* **2018**, *8* (1), 1–8. https://doi.org/10.1038/s41598-018-33205-4.

(38) Xu, L.; Dong, Y.; Xu, W.; Zhang, W. Ultrafast and Facile Synthesis of (Ni/Fe/Mo)OOH on Ni Foam for Oxygen Evolution Reaction in Seawater Electrolysis. *Catalysts* **2023**, *13* (6). https://doi.org/10.3390/catal13060924.

(39) Xu, L.; Cao, L.; Xu, W.; Pei, Z. One-Step Electrosynthesis of NiFe-NF Electrodes for Highly Efficient Overall Water Splitting. *Appl. Surf. Sci.* **2020**, *503*. https://doi.org/10.1016/j.apsusc.2019.144122.

(40) Gupta, S.; Patel, N.; Fernandes, R.; Kadrekar, R.; Dashora, A.; Yadav, A. K.; Bhattacharyya, D.; Jha, S. N.; Miotello, A.; Kothari, D. C. Co-Ni-B Nanocatalyst for Efficient Hydrogen Evolution Reaction in Wide PH Range. *Appl. Catal. B Environ.* **2016**, *192*, 126–133. https://doi.org/10.1016/j.apcatb.2016.03.032.

(41) Giannozzi, P.; Baroni, S.; Bonini, N.; Calandra, M.; Car, R.; Cavazzoni, C.; Ceresoli,

D.; Chiarotti, G. L.; Cococcioni, M.; Dabo, I.; Dal Corso, A.; De Gironcoli, S.; Fabris, S.; Fratesi, G.; Gebauer, R.; Gerstmann, U.; Gougoussis, C.; Kokalj, A.; Lazzeri, M.; Martin-Samos, L.; Marzari, N.; Mauri, F.; Mazzarello, R.; Paolini, S.; Pasquarello, A.; Paulatto, L.; Sbraccia, C.; Scandolo, S.; Sclauzero, G.; Seitsonen, A. P.; Smogunov, A.; Umari, P.; Wentzcovitch, R. M. QUANTUM ESPRESSO: A Modular and Open-Source Software Project for Quantum Simulations of Materials. *J. Phys. Condens. Matter* **2009**, *21* (39). https://doi.org/10.1088/0953-8984/21/39/395502.

(42) Perdew, J. P.; Burke, K.; Ernzerhof, M. Generalized Gradient Approximation Made Simple. *Phys. Rev. Lett.* **1996**, *77* (18), 3865–3868. https://doi.org/10.1103/PhysRevLett.77.3865.

(43) Laasonen, K.; Pasquarello, A.; Car, R.; Lee, C.; Vanderbilt, D. Car-Parrinello Molecular Dynamics with Vanderbilt Ultrasoft Pseudopotentials. *Phys. Rev. B* **1993**, *47* (16), 10142–10153. https://doi.org/10.1103/PhysRevB.47.10142.

(44) Harada, Y.; Ikuhara, Y. The Latest Analytical Electron Microscope and Its Application to Ceramics. In *Handbook of Advanced Ceramics: Materials, Applications, Processing, and Properties: Second Edition*; Elsevier Inc., 2013; pp 3–21. https://doi.org/10.1016/B978-0-12-385469-8.00001-0.

(45) Patel, N.; Fernandes, R.; Bazzanella, N.; Miotello, A. Co-P-B Catalyst Thin Films Prepared by Electroless and Pulsed Laser Deposition for Hydrogen Generation by Hydrolysis of Alkaline Sodium Borohydride: A Comparison. *Thin Solid Films* **2010**, *518* (17), 4779–4785. https://doi.org/10.1016/j.tsf.2010.01.029.

(46) Larrude, D. G.; Maia Da Costa, M. E. H.; Monteiro, F. H.; Pinto, A. L.; Freire, F. L. Characterization of Phosphorus-Doped Multiwalled Carbon Nanotubes. *J. Appl.*

Phys. **2012**, *111* (6), 0–6. https://doi.org/10.1063/1.3695452.

(47) Liang, H. W.; Brüller, S.; Dong, R.; Zhang, J.; Feng, X.; Müllen, K. Molecular Metal-Nx Centres in Porous Carbon for Electrocatalytic Hydrogen Evolution. *Nat. Commun.* **2015**, *6*, 1–8. https://doi.org/10.1038/ncomms8992.

(48) Zhang, K.; Zou, R. Advanced Transition Metal-Based OER Electrocatalysts: Current Status, Opportunities, and Challenges. *Small*. 2021, pp 1–40. https://doi.org/10.1002/smll.202100129.

(49) Xu, P.; Li, J.; Luo, J.; Wei, L.; Zhang, D.; Zhou, D.; Xu, W.; Yuan, D. (Fe0.2Ni0.8)0.96S Tubular Spheres Supported on Ni Foam as an Efficient Bifunctional Electrocatalyst for Overall Water Splitting. *Sci. Rep.* **2018**, *8* (1), 1–9. https://doi.org/10.1038/s41598-018-27477-z.

(50) Candelaria, S. L.; Bedford, N. M.; Woehl, T. J.; Rentz, N. S.; Showalter, A. R.; Pylypenko, S.; Bunker, B. A.; Lee, S.; Reinhart, B.; Ren, Y.; Ertem, S. P.; Coughlin, E. B.; Sather, N. A.; Horan, J. L.; Herring, A. M.; Greenlee, L. F. Multi-Component Fe-Ni Hydroxide Nanocatalyst for Oxygen Evolution and Methanol Oxidation Reactions under Alkaline Conditions. *ACS Catal.* **2017**, *7* (1), 365–379. https://doi.org/10.1021/acscatal.6b02552.

(51) Gupta, S.; Yadav, A.; Bhartiya, S.; Singh, M. K.; Miotello, A.; Sarkar, A.; Patel, N. Co Oxide Nanostructures for Electrocatalytic Water-Oxidation: Effects of Dimensionality and Related Properties. *Nanoscale* **2018**, *10* (18), 8806–8819. https://doi.org/10.1039/c8nr00348c.

(52) Du, J.; Li, C.; Wang, X.; Jones, T. G. J.; Liang, H. P. Cobalt Oxyhydroxide with Highly Porous Structures as Active and Stable Phase for Efficient Water Oxidation.

Electrochim. Acta **2019**, *303*, 231–238. https://doi.org/10.1016/j.electacta.2019.02.083.

(53) Man, I. C.; Su, H. Y.; Calle-Vallejo, F.; Hansen, H. A.; Martínez, J. I.; Inoglu, N. G.; Kitchin, J.; Jaramillo, T. F.; Nørskov, J. K.; Rossmeisl, J. Universality in Oxygen Evolution Electrocatalysis on Oxide Surfaces. *ChemCatChem* **2011**, *3* (7), 1159–1165. https://doi.org/10.1002/cctc.201000397.

(54) Christensen, R.; Hansen, H. A.; Dickens, C. F.; Nørskov, J. K.; Vegge, T. Functional Independent Scaling Relation for ORR/OER Catalysts. *J. Phys. Chem. C* **2016**, *120* (43), 24910–24916. https://doi.org/10.1021/acs.jpcc.6b09141.

(55) Franco-Pérez, M.; Gázquez, J. L. Electronegativities of Pauling and Mulliken in Density Functional Theory. *J. Phys. Chem. A* **2019**, *123* (46), 10065–10071. https://doi.org/10.1021/acs.jpca.9b07468.

(56) Badreldin, A.; Abusrafa, A. E.; Abdel-Wahab, A. Oxygen-Deficient Cobalt-Based Oxides for Electrocatalytic Water Splitting. *ChemSusChem* **2021**, *14* (1), 10–32. https://doi.org/10.1002/cssc.202002002.